Mon. Not. R. Astron. Soc. **000**, 1–15 (2000)   Printed 31 August 2000   (MN LaTeX style file v1.4)

Kinematics of the Gum nebula region

Beate Woermann[1,2]*, Michael J. Gaylard[1] and Robina Otrupcek[3]
[1]*Hartebeesthoek Radio Astronomy Observatory, PO Box 443, Krugersdorp 1740, South Africa*
[2]*Department of Physics & Electronics, Rhodes University, Grahamstown 6140, South Africa*
[3]*Australia Telescope National Facility, PO Box 76, Epping, NSW 2121, Australia*

Accepted 2000. Received 2000 ; in original form 2000

ABSTRACT

To investigate the kinematics of the neutral material around the Gum nebula, emission from hydroxyl at 1667 MHz was observed at many positions over the region. Fitting models of expanding shells to these data together with previously published molecular line data shows that the diffuse molecular clouds and cometary globules form a single expanding shell centred on G261−2.5. The mean angular radius is 10.5° and its maximum radius is 14°. The models show that the distance range to the expansion centre is 200 pc to 500 pc.

The path of the runaway O-star ζ Puppis passed within $< 0.5°$ of the expansion centre of the neutral shell ∼1.5 Myr ago. The supernova of the erstwhile binary companion of ζPuppis is the probable origin of the Gum nebula and the swept up expanding neutral shell. The 500 pc distance to the supernova is adopted as the distance to the expansion centre of the neutral shell. At this distance the energy requirement to produce the observed expansion could have been met with a single supernova. The radii of the front and back faces of the shell are 130 pc and 70 pc respectively. The front face is expanding faster than the back face, at 14 km s^{-1} and 8.5 km s^{-1} respectively.

The extent of the neutral shell matches the radio continuum and Hα emission of the Gum nebula well. The photo-ionized gas in the nebula is probably primarily ionized by ζ Puppis, which is still within the neutral shell. No evidence was found for the IRAS-Vela shell as a separate expanding shell.

Key words: ISM: individual: Gum nebula – ISM: individual: IRAS-Vela shell – ISM: molecules – ISM: kinematics – ISM: supernova remnants – ISM: HII regions – stars: individual: ζ Puppis

1 INTRODUCTION

The Gum nebula was discovered on large area Hα photographs of the southern Milky Way (Gum 1952). The subsequent controversy about its angular size was settled by Chanot & Sivan (1983) on the basis of narrowband, long exposure Hα photographs. The main body of the nebula is $\sim 36°$ in diameter and is approximately centred on G258−2.

Previous research has produced conflicting results regarding the kinematics of the Gum nebula and its surroundings. We have obtained new molecular line data and developed new models to address these issues, which are defined below.

- **The Gum nebula and IRAS-Vela shell**

Sahu (1992) proposed that the IRAS-Vela shell (IVS) surrounds the Vela OB2 association, including the WC8+O binary star γ^2Velorum at G262.8−7.7. The parameters they deduced for the IVS are: centre at G263−7, angular radius of 8°, distance of 450 pc (the then accepted distance to the Vela OB2 association). The Hipparcos distance estimate to γ^2Velorum is 258^{+41}_{-31} pc (van der Hucht et al. 1997) and to the OB2 association is 410 pc (De Zeeuw et al. 1999). However it has been argued post-Hipparcos that γ^2 Velorum may be as far from us as the Vela OB2 association (Pozzo et al. 2000).

The IVS is smaller than the Gum nebula and lies within its boundary as seen from Earth. While proposed as a separate entity seen superimposed on the Gum nebula, it could simply be a density enhancement of the Gum nebula.

Woermann (1998) showed that the ratio of mid-infrared to radio flux over the IVS is not significantly different from that over the rest of the Gum nebula. In addition, the distribution of the 60-μm infrared emission over the Gum nebula above the galactic plane follows much of the radio and Hα morphology of the nebula. This indicates that the two

* E-mail: beate@hartrao.ac.za

objects cannot be distinguished by the absence of infrared emission in the case of the Gum nebula, or its presence in the case of the IRAS-Vela shell, as suggested by Sahu (1992) and Sahu & Sahu (1993).

However, the postulate that the IVS is a separate object hinges on understanding the kinematics of the whole region.

- **Expansion of the Gum nebula**

Sahu (1992) and Sahu & Sahu (1993) detected double component [NII] line spectra only in the IVS region, which was interpreted as evidence that this shell is expanding at 10 ± 2 km s^{-1}. Positions outside the IVS but within the Gum nebula showed only single line components, from which they inferred that the Gum nebula is not expanding and is an entirely separate entity to the IVS. Hippelein & Weinberger (1975) and Wallerstein, Jenkins & Silk (1980) had also seen no evidence for expansion of the Gum nebula.

However, in apparent conflict with this, Reynolds (1976a) had observed double emission line spectra of [NII] at G253.3+8.5, G255.6+6.4 and G263.8+6.0 within the Gum Nebula but outside the IVS. He found that the nebula is expanding at ∼20 km s^{-1}.

Rajagopal & Srinivasan (1998) associated the molecular material they detected in CO with the IRAS-Vela shell (IVS), which they determined to be expanding at 13 km s^{-1}. Yamaguchi et al. (1999) also observed CO, but they deduced that the molecular material is associated with the Gum nebula and is expanding at 10 to 15 km s^{-1}. As the CO data used by Rajagopal & Srinivasan (1998) and Yamaguchi et al. (1999) cover essentially the same angular extent, this leaves unresolved the questions of the relationship between the Gum nebula and IVS and the possible expansion of each object.

- **The Cometary globules**

Cometary globules (CGs) are distributed over the area of the IVS and the Gum nebula. They could be associated with either object, or have an independent origin. Sridharan (1992) noted that the mean radius of the CG shell is ∼9.5°, similar to the 8° radius of the IVS and substantially smaller than the 18° radius of the Gum nebula. Nevertheless many of the CGs are positioned well outside the IVS.

Centres of expansion previously derived for the CGs include G261−5 (Reipurth 1983), G261.2−5.2, G260.3−10.6 and G261.1−4.5 (Zealey et al. 1983) and G260.2−4.0 (Sridharan 1992). Taking an average gives a centre position of G260.8−5.9. This is ∼4.8° from the Hα centre of the Gum nebula at G258−2 (Chanot & Sivan 1983) and ∼2.5° from the centre of the IVS at G263−7 (Sahu 1992, Sahu & Sahu 1993), and hence does not provide a definitive answer to the question of association with either object, but does not exclude such association.

If the CGs are part of the Gum nebula or of the IVS they should share the kinematics of the associated object. Zealey et al. (1983) measured the velocities of fifteen formaldehyde absorption lines from CGs and found that the velocity residuals after subtracting large scale kinematics could only be explained by a shell with an expansion velocity of up to 5 km s^{-1}. Sridharan (1992) detected CO in 34 positions on the CGs and showed that the CO velocities are consistent with a shell of ∼9.5° radius expanding at 12 km s^{-1}, if it is assumed that the CGs are distributed over a volume within the shell rather than on its surface. The latter is similar to the result of Yamaguchi et al. (1999) and Rajagopal & Srinivasan (1998) for the Gum nebula and the IVS respectively, leaving the question of the object with which the CGs are associated unanswered. This is not unexpected, as all kinematic models of the objects used assumed expansion centres and distances. For example, Yamaguchi et al. (1999) assume that the expansion centre is G260−3 and distance 500 pc. Sridharan (1992) uses a centre position of G260−4 and distance 450 pc, and this is also used by Rajagopal & Srinivasan (1998).

Here we attempt to obtain definitive answers to these questions. The approach taken is to test the fit of molecular line data to expanding shell models. No assumptions are made about the centre position, angular size and distance of the shells, to avoid *a priori* bias.

In section 2 we discuss the choice of positions for obtaining new 1667 MHz hydroxyl (OH) line data for these tests, to supplement published data. The observations are described in section 3, and the results in section 4. The uniform expansion model is covered in section 5. The geometry is discussed in section 5.1, data selection in section 5.2, testing the diffuse molecular cloud and cometary globule data with the model in section 5.3, modelling the IVS in section 5.4, and the uniformity of the shell expansion in section 6. Section 7 covers possible non-uniform expansion of the shell. The geometry of the model for non-uniform expansion is described in section 7.1, and fitting it to the data and possible origins of the shell are covered in 7.2. The nature of the Gum nebula and molecular clouds as seen at different wavelengths and their origin are discussed in section 8. Conclusions follow in section 9.

2 POSITION SELECTION FOR HYDROXYL LINE OBSERVATIONS

The radial component of the expansion velocity of a shell is largest on the line of sight through the expansion centre, assuming uniform spherical expansion. Hence we wished to select positions close to the centre of the nebula. However, published data and test observations showed that confusion with other sources becomes significant within ∼4° of the galactic plane, and this zone was therefore excluded. Observing positions were spaced along three lines radiating from near the geometric centre of the Gum nebula at G258−2 (Chanot & Sivan, 1983) to its edge (Fig. 1). One of these radials crosses the IVS and passes close to its centre. Complete coverage of the nebula was not attempted owing to its size compared to telescope beam sizes of ∼30′ and the faintness of the emission.

Detection of molecular material in this region is not guaranteed, as Goss et al. (1980), de Vries et al. (1984) and Zealey et al. (1983) had shown. Thus criteria for selecting positions that favour detections were applied. The 60-μm IRAS map (Wheelock et al. 1994) was used to isolate positions with high infrared intensity and the dark cloud catalogues (Feitzinger & Stüwe 1984, Hartley et al. 1986) were used to identify concentrations of molecular material. Some additional points away from the radials were also selected using these criteria. The infrared emission above the galactic plane is weak and no dark clouds are listed there, so only a few positions were observed in this region.

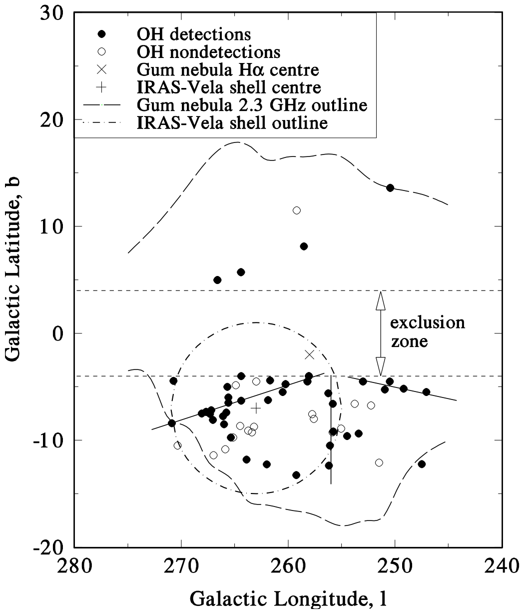

Figure 1. Circles mark the positions observed in the OH 1667 MHz line. Their size is approximately equal to the beam size. The solid lines indicate the three radials along which most observations were made. The outline of the 2.3-GHz radio emission (Jonas, Baart & Nicolson 1998) from the Gum nebula, its optical centre, and the IVS centre and outline are shown. No observations were made in the exclusion zone within $|b| < 4°$.

3 OBSERVATIONS

Observations were made in the frequency-switching mode with the 18-cm system on the 26-m antenna at the Hartebeesthoek Radio Observatory (HartRAO), South Africa and the 20-cm system on the 22-m Mopra antenna of the ATNF in Australia.

The observations at HartRAO were made in one polarization only i.e. left-hand circularly polarized. Spectra were obtained in 1992 and 1993. The average zenith system temperature of the HartRAO system was 45 K and its point source sensitivity was 10 $\mathrm{JyK^{-1}}$ as measured on Hydra A. The beamwidth of the antenna is $30'$. Several different correlator bandwidths were used, giving spectral resolutions from 0.5 to 2.2 km $\mathrm{s^{-1}}$.

The 20-cm receiver system at Mopra provided simultaneous left- and right-hand circular polarizations. The average zenith system temperature was 34 K at 1665 MHz for both polarizations. The point source sensitivity was 12.7 Jy $\mathrm{K^{-1}}$, as measured on Virgo A (A. Tzioumis, private communication). At 1665 MHz the half power beamwidth of the Mopra antenna is $33'$. The observations were made in 1994 February and March. The spectra have a velocity resolution of 0.84 km $\mathrm{s^{-1}}$.

4 RESULTS

Line parameters were determined by fitting Gaussian profiles. Spectra with low signal-to-noise ratios were first smoothed with the Hamming function. The resultant velocity resolutions are listed in Tables 1 and 2 together with the position in galactic coordinates l, b, the line antenna temperature T_A, the line velocity with respect to the local standard of rest v_{lsr} and the line width Δv.

Table 1. The line parameters of Gaussian fits to the OH 1667 MHz spectra obtained at HartRAO. For non-detections an upper limit on the line antenna temperature is given.

l [°]	b [°]	vel. resol. [km $\mathrm{s^{-1}}$]	T_A [mK]	v_{lsr} [km $\mathrm{s^{-1}}$]	Δv [km $\mathrm{s^{-1}}$]
247.50	−12.23	0.5	65 ± 6	+2.6 ± 0.1	1.7 ± 0.2
247.07	−5.50	2.2	33 ± 4	+21.1 ± 0.3	4.1 ± 0.7
249.20	−5.18	1.1	33 ± 2	+21.0 ± 0.2	7.7 ± 0.4
250.45	+13.60	1.1	≤20		
250.50	−4.50	1.1	40 ± 3	+18.8 ± 0.2	5.7 ± 0.5
250.95	−5.25	1.1	30 ± 3	+17.6 ± 0.3	6.0 ± 0.9
			22 ± 5	+24.4 ± 0.3	1.7 ± 0.4
251.50	−12.10	2.2	≤20		
252.25	−6.75	1.1	≤16		
254.50	−9.60	0.5	34 ± 3	−1.7 ± 0.1	2.3 ± 0.2
255.85	−9.25	1.1	≤20		
256.10	−10.50	0.5	42 ± 4	−2.2 ± 0.1	2.4 ± 0.3
256.20	−12.38	1.5	18 ± 2	−1.7 ± 0.2	3.1 ± 0.4
257.60	−8.00	1.1	≤20		
259.20	+11.50	1.1	≤20		
259.25	−13.25	0.3	70 ± 9	+5.1 ± 0.1	0.9 ± 0.1
260.25	−4.75	1.1	12 ± 2	+3.7 ± 0.4	3.8 ± 0.9
			19 ± 2	+11.6 ± 0.2	3.8 ± 0.6
262.00	−12.25	1.5	22 ± 2	+5.2 ± 0.1	2.3 ± 0.2
263.40	−9.25	1.1	≤25		
263.90	−11.80	1.1	33 ± 19	+3.7 ± 0.1	≤ 0.45
264.40	−4.00	2.2	30 ± 3	+3.9 ± 0.2	1.9 ± 0.4
264.90	−4.85	2.2	≤10		
265.15	−9.75	1.1	≤10		
265.60	−6.00	1.1	21 ± 2	+5.0 ± 0.2	4.7 ± 0.6
266.10	−7.75	1.1	116 ± 19	+3.5 ± 0.1	0.9 ± 0.4
267.05	−8.10	1.5	17 ± 2	+1.7 ± 0.2	3.8 ± 0.4
268.10	−7.50	0.5	24 ± 2	+3.9 ± 0.2	3.9 ± 0.4
270.35	−10.50	1.1	≤20		
270.75	−4.45	1.1	23 ± 3	+2.2 ± 0.5	8.0 ± 1.0
270.90	−8.40	0.5	29 ± 3	+0.3 ± 0.1	2.4 ± 0.3

The unsmoothed 1667 MHz spectra from HartRAO and Mopra are shown in Fig. 2 and 3 respectively. In some spectra there appear to be more lines present than tabulated. The unlisted lines have a signal-to-noise ratio too low to confirm their reality. Confirming their existence would require at least doubling the integration time. In cases where multiple lines are present, the minimum number of Gaussians was fitted. Thus we list several low intensity broad lines that may well be made up of several narrower lines.

The method used to fit an expansion model in a least squares sense to the data is covered in the following section.

5 MODELS OF UNIFORMLY EXPANDING SHELLS

5.1 Shell geometry

The geometry of a spherically symmetric shell of material expanding radially from its centre with a velocity v_{exp} is shown in Fig. 4a. The centre lies at a distance D from the observer. For spherical, uniform expansion of a shell of physical radius R, we have $\sin\theta_{max} = R/D$, where θ_{max} is the angular radius. A spectral line with radial velocity v_{rad} is detected at a position on the shell an angular distance θ from the centre of the shell. The angle θ is calculated using the spherical trigonometric cosine formula in the galactic coordinate system. θ was assigned a negative or positive value depending on whether the galactic latitude of the observed

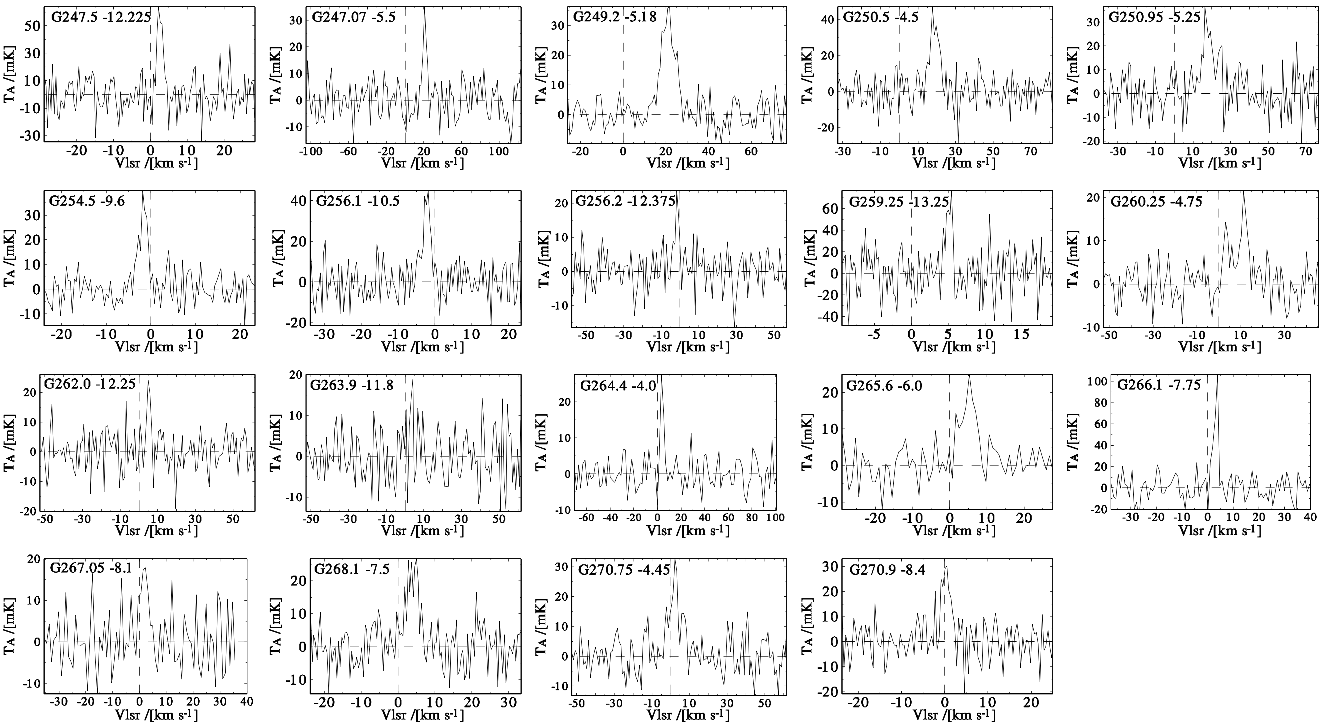

Figure 2. The OH 1667 MHz detections from observations made at HartRAO.

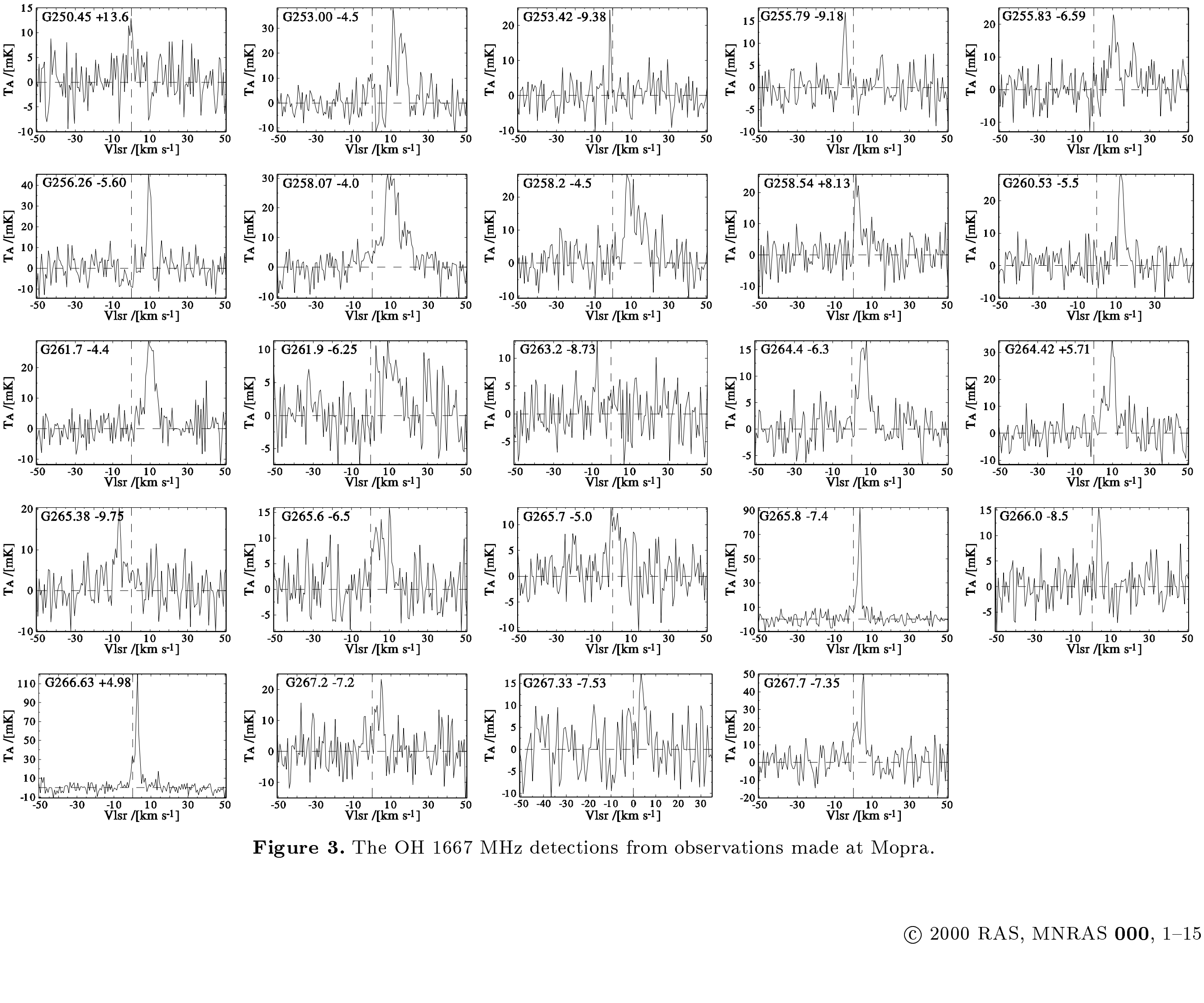

Figure 3. The OH 1667 MHz detections from observations made at Mopra.

Table 2. The line parameters of gaussian fits to the OH 1667 MHz spectra obtained at Mopra. For non-detections an upper limit for the line antenna temperature is given.

l [°]	b [°]	vel. resol. [km s^{-1}]	T_A [mK]	v_{lsr} [km s^{-1}]	Δv [km s^{-1}]
250.45	+13.60	1.14	10 ± 2	−0.3 ± 0.2	3.6 ± 0.9
253.00	−4.50	0.84	27 ± 2	+16.2 ± 0.2	4.0 ± 0.4
			38 ± 3	+11.4 ± 0.1	1.7 ± 0.2
253.42	−9.38	0.84	37 ± 14	−1.2 ± 0.1	≤ 0.5
253.78	−6.60	0.84	≤17		
255.06	−8.91	0.84	≤10		
255.79	−9.18	0.84	17 ± 2	−4.5 ± 0.1	2.0 ± 0.3
255.83	−6.59	0.84	18 ± 2	+10.9 ± 0.2	4.4 ± 0.6
			11 ± 5	+21.1 ± 0.8	3.6 ± 2.7
256.26	−5.60	0.84	46 ± 3	+9.6 ± 0.1	2.1 ± 0.2
257.75	−7.55	0.84	≤8		
258.07	−4.00	0.84	22 ± 2	+10.2 ± 0.2	6.0 ± 0.6
			11 ± 1	+11.5 ± 0.7	27 ± 3
258.20	−4.50	1.14	17 ± 2	+8.1 ± 0.2	3.0 ± 0.5
			14 ± 1	+13.0 ± 0.6	11 ± 1
258.54	+8.13	0.84	25 ± 2	+2.1 ± 0.2	2.8 ± 0.3
260.53	−5.50	0.84	29 ± 2	+12.6 ± 0.1	3.1 ± 0.3
261.70	−4.40	0.84	27 ± 2	+10.3 ± 0.2	5.9 ± 0.4
261.90	−6.25	1.14	8 ± 1	+10.3 ± 0.4	10.9 ± 0.7
			8 ± 1	+30.0 ± 0.2	3.2 ± 0.4
263.00	−4.50	0.84	≤10		
263.20	−8.73	0.84	≤14		
263.75	−9.10	0.84	≤12		
264.40	−6.30	0.84	16 ± 1	+6.3 ± 0.2	5.8 ± 0.5
264.42	+5.71	1.14	33 ± 2	+10.1 ± 0.1	2.9 ± 0.2
			14 ± 1	+5.4 ± 0.2	3.2 ± 0.5
264.50	−8.65	0.84	≤12		
265.38	−9.75	0.84	14 ± 2	−6.7 ± 0.3	4 ± 1
265.60	−6.50	0.84	10 ± 1	+5.6 ± 0.6	11 ± 1
265.70	−5.00	0.84	11 ± 1	+1.3 ± 0.4	6 ± 1
265.80	−7.40	0.84	84 ± 3	+3.4 ± 0.1	1.7 ± 0.1
265.90	−10.85	0.84	≤14		
266.00	−8.50	0.84	17 ± 2	+3.7 ± 0.1	1.7 ± 0.2
266.63	+4.98	0.84	90 ± 4	+2.7 ± 0.1	0.9 ± 0.1
			34 ± 3	+1.9 ± 0.2	5.2 ± 0.4
267.00	−11.40	0.84	≤12		
267.20	−7.20	1.14	16 ± 1	+3.8 ± 0.2	4.7 ± 0.5
267.33	−7.53	1.14	14 ± 2	+3.9 ± 0.2	3.5 ± 0.8
267.70	−7.35	0.84	23 ± 3	+1.5 ± 0.3	3.3 ± 0.6
			52 ± 5	+5.3 ± 0.1	1.4 ± 0.2

position was less than or greater than the latitude of the centre of the shell.

The observed line is doppler-shifted from its rest frequency, giving v_{res}, the component of the expansion velocity of the shell along the line of sight. The observed radial velocity, v_{rad}, is the sum of v_{res} and v_{gal}, the component along the line of sight of the differential galactic rotation for an object at distance S.

From the viewing geometry depicted in Fig. 4a, the line of sight component of the expansion velocity, v_{res}, is given by :

$$v_{res} = \pm v_{exp}(1 - D^2 \sin^2\theta / R^2)^{\frac{1}{2}} \quad (1)$$

where the plus sign applies to a line emitted from the back face of the shell and the minus sign applies to a line emitted from the front face. For a spherical, uniformly expanding shell, where $R = D \sin\theta_{max}$, a plot of v_{res} versus $(1 - \sin^2\theta / \sin^2\theta_{max})^{\frac{1}{2}}$ results in the bimodal distribution shown in fig. 8b of Sridharan (1992). A version of this plot is used by Sridharan (1992) and Rajagopal & Srinivasan (1998) for their expansion models.

Solving for $\sin\theta$ in Equation 1 we obtain the form of the expansion model used here:

$$\sin\theta = \pm \sin\theta_{max}(1 - v_{res}^2 / v_{exp}^2)^{\frac{1}{2}}. \quad (2)$$

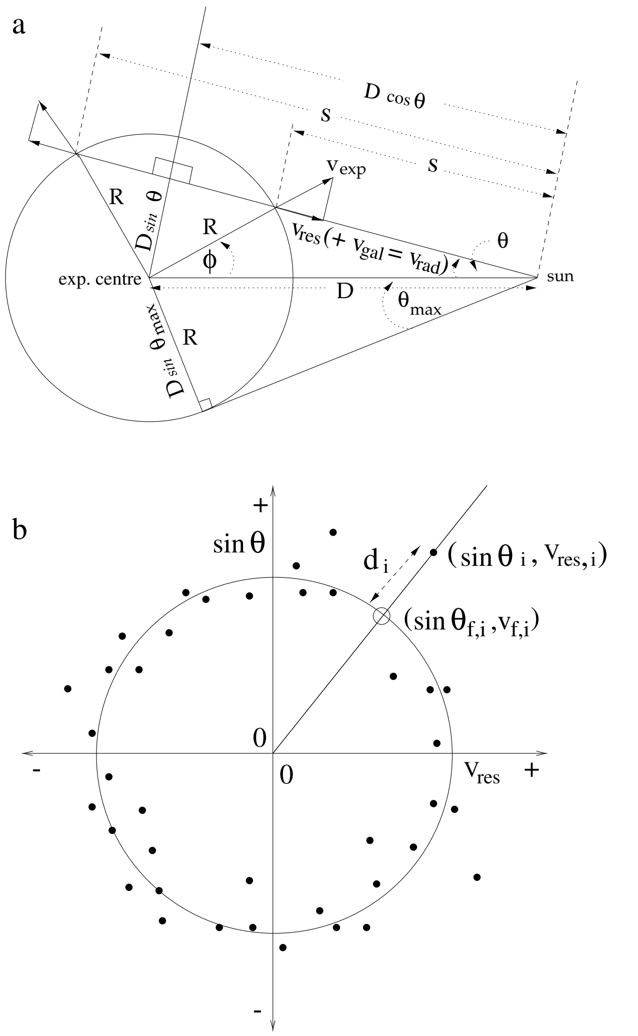

Figure 4. a. Schematic diagram of the viewing geometry of a spectral line observed at a position on the near or far face of a spherical, uniformly expanding shell. b. Graph of $\sin\theta$ versus the residual velocity v_{res}, showing the scatter of the data points about the curve representing Equation 2 with the best fit parameters.

The solid line in Fig. 4b is an idealised plot of $\sin\theta$ versus the residual velocity, v_{res}. In practise the shell will have a finite thickness and will be clumpy rather than homogeneous, giving some peculiar velocity at each point, relative to the overall expansion velocity. Thus the observed data points are scattered about the best fit line, as shown.

The least-squares fit to the data of the expansion model with a particular value of R, D and v_{exp} was obtained as follows. The intersection point $(\sin\theta_{f,i}, v_{f,i})$ of the straight line passing through the two points $(0, 0)$ and $(\sin\theta_i, v_{res,i})$, as shown in Fig. 4b, and the function given by Equation 2 is given by:

$$v_{f,i} = \pm \left[(\sin^2\theta_{max} v_{exp}^2)/(\sin^2\theta_{max} + v_{exp}^2(\sin\theta_i / v_{res,i})\right]^{\frac{1}{2}} \quad (3)$$

$$\sin\theta_{f,i} = (\sin\theta_i / v_{res,i}) v_{f,i} \quad (4)$$

where $v_{f,i}$ has the same sign as $v_{res,i}$. For the best fit, the square root of the sum of the square of the distances d_i (Fig. 4b) is a minimum. Thus the reduced χ^2_ν to be minimized in determining the best fit of Equation 2 to the N data points $(\sin\theta_i, v_{res,i})$ with their associated standard deviations σ_i is

$$\chi^2_\nu = \Sigma^N_{i=1}[(\sin\theta_i - \sin\theta_{f,i})^2 + (v_{res,i} - v_{f,i})^2]/\sigma^2_i\nu \qquad (5)$$

where ν is the number of degrees of freedom given by the number of data points N minus the number of parameters of the distribution determined from those data points. We assumed that all points have equal weight, i.e. that $\sigma = 1$ for all data points.

Equation 5 assumes that the scale on the two axes is the same. As $\sin\theta$ and v_{res} have different units this is not the case, effectively weighting the velocity component of the points far more than the angular component. By scaling the $\sin\theta$ axis consistently by fifty, as indicated in plots of this type (Fig. 4b), we gave approximately equal weighting to the two axes.

The best-fit expansion velocity, expansion centre, angular radius and distance to the nebula (obtained indirectly through the contribution of the galactic rotation velocity to the observed radial velocity) are given by the values that give rise to the minimum χ^2. Confidence limits for each of these parameters may be obtained by use of constant χ^2 boundaries. 1-σ, 2-σ and 3-σ confidence levels are given by projecting, onto the axis of the parameter of interest, the region in parameter space that encloses all χ^2 that differ from the minimum χ^2 by a $\Delta\chi^2$ of 1, 4 and 9 respectively (Press et al. 1992). χ^2 was evaluated for plausible ranges of the expansion velocity, centre position and angular radius, in order to find the minima and confidence levels.

Observed positions whose angular distance θ from the centre of the shell is less than θ_{max}, the radius of the shell, may lie on either the front or the rear face of the shell. The distance, S, to the position on the shell is then derived geometrically from Fig. 4a, as

$$S = D\cos\theta \pm (D^2(\sin^2\theta_{max} - \sin^2\theta))^{\frac{1}{2}} \qquad (6)$$

where the minus sign is for clouds on the front face and the plus sign for those on the back face. The distance ambiguity was resolved by assigning the near distance if the radial velocity due to galactic rotation at that position with a heliocentric distance $D\cos\theta$ is larger than the observed velocity and vice versa. The flat galactic rotation model of Fich, Blitz & Stark (1989) with $R_o = 8.5$ kpc and $\Theta_o = 220$ km s^{-1} was used to calculate the contribution of galactic rotation to the observed radial velocity, using the appropriate distance S given by Equation 6. Their flat rotation curve gives practically identical distance values to those given by their linear fit rotation curve, provided that the correct Ω_o, i.e. 221.641 km s^{-1} as given in their Equation 23, is used for the linear fit. For positions with $\theta > \theta_{max}$, which occurs because θ_{max} is the mean angular radius, a distance to the cloud of $D\cos\theta$ was assumed.

5.2 Selection of data for expansion model tests

Published data on molecular lines not specifically associated with cometary globules were combined with the 1667 MHz OH data obtained here. For simplicity, sources of this emission are here called diffuse molecular clouds (DMCs) to differentiate them from the cometary globules (CGs).

To obtain data points that were statistically independent, a representative value of the line velocity was adopted for observed positions that were identical or similar in the various data sources, taking into account the velocity resolution of the data and the beam sizes used for the observations. Table 3 lists the compiled molecular line data in the Gum nebula region, excluding the data from cometary globules and from positions within galactic latitude $\pm4°$.

Previous molecular line observations of the CGs were combined in a similar way to produce the data set shown in Table 4. Inconsistencies in the data for CGs 16 and 17 were resolved by inspection of the CO spectra of Otrupcek et al. (2000). As they have been identified optically, CGs within $\pm4°$ of the galactic plane were not excluded from the sample.

5.3 Modelling the DMC and CG data

During the fitting process the DMC data were tested for outliers, i.e. clouds that did not share the motion of the majority of the DMCs. This was done as follows. The uniformly expanding shell model was fitted to the DMC data for the parameter ranges and intervals given in Table 5. Data lying more than 3.5σ from the best-fit model were discarded. This process was repeated until no more data points needed to be discarded. We returned to the original data set in a final run using the parameter values from the final iteration. The final set of data excluded as outliers comprised those points that were further than 2.5σ from that best-fit model. The excluded data points have been marked by an asterisk in Table 3. The DMC data set used hereafter excludes these outliers. The identified outliers comprise only 15 of the total of 100 data points used for the fit.

Five of the outliers form a group lying between G247.0−5.7 and G253.0−4.5 with velocities in the range +21.1 to +16.2 kms^{-1}. Their velocities suggest that they lie at a distance of ~2 kpc. The three at high latitudes (G247.5−12.25, 250.45+13.6 and G264.5−11.3) appear to be unrelated cirrus. The remaining five, from G260.25−4.75 to G265.7−5.0, lie just below the latitude range from which DMC data were excluded. They are probably from molecular clouds on the far side of the shell, perhaps associated with the Vela molecular ridge (Murphy & May 1991).

Table 6 gives the minimum reduced χ^2 found within the parameter ranges given in Table 5 for the DMC data set listed in Table 3. The uniformly expanding shell that best fits the DMC data is shown in Fig. 5a. While the fit is plausible, there are no points in the front face with $v_{res} < -7$ km s^{-1}, and the shell is poorly sampled at positive θ. In both cases this may represent a true dearth of molecular material, but the exclusion of data in the confusion zone within $\pm4°$ of the Galactic plane will have contributed to this.

If the CGs are part of the same expanding shell defined by the DMCs, the best-fit of a uniformly expanding shell model to the CG data set should give similar parameter values to that for the DMCs. This fit is shown in Fig. 5b and its parameter values are listed in Table 6. No CGs are found in the back face. However the extreme front face is also poorly represented in this data set. As all CG data were included irrespective of whether they lie within 4° of the plane, this is the true distribution on the shell of the known CGs.

The best fit distances to the expansion centres are 200 pc apart, raising the possibility that these are therefore two

Table 3. The positions and adopted line velocities of diffuse molecular clouds. Positions labelled with a * were identified as outliers in the shell-fitting process.

l [°]	b [°]	v_{lsr} [km s^{-1}]	refs.[a]	l [°]	b [°]	v_{lsr} [km s^{-1}]	refs.[a]	l [°]	b [°]	v_{lsr} [km s^{-1}]	refs.[a]
247.00	−5.70*	+20.6	1	258.90	−4.10	+8.5	1	266.00	−4.30	+4.9	1
247.07	−5.50*	+21.1	2	259.00	−13.20	+4.4	1	266.02	+4.32	+1.5	3
247.50	−12.25*	+2.5	1,2	259.10	−4.00	+9.5	1	266.10	−7.75	+3.5	1,2,6
249.20	−5.18*	+21.0	2	259.25	−13.25	+5.2	1,2,6	266.63	+4.98	+1.9	4
249.40	−5.10*	+18.2	1	259.90	−4.40	+9.6	1	266.63	+4.98	+2.6	1,4
249.42	−5.10	+7.5	1,3	260.25	−4.75*	+3.7	2	267.05	−8.10	+1.7	2
250.45	+13.60*	−0.3	4	260.25	−4.75	+11.6	2	267.15	−7.20	+4.9	1,4,5,7
250.50	−4.50*	+18.8	2	260.40	−8.00*	+3.4	1	267.30	−7.32	+5.9	7
250.80	−8.10	−1.0	1	264.40	−4.00*	+3.9	2	267.39	−7.51	+5.3	3,4,5,6,7
250.95	−5.25*	+18.2	2	260.50	−5.20*	+5.0	1	267.40	−7.50	+8.6	1
251.70	−12.20	−1.3	1	260.53	−5.50	+12.6	4	267.46	−7.39	+6.0	5,7
253.00	−4.50*	+16.2	4	260.60	−12.70	−2.4	1	267.60	−7.40	+5.6	1
253.20	−4.25	+11.6	1,4	261.70	−12.50	+6.1	1	267.60	−6.40	+5.7	1,5
253.42	−9.38	−1.2	4	261.70	−4.40	+10.3	1,4	267.60	−6.00	+5.8	1,5
253.80	−10.90	−1.2	1,5	261.90	−6.25	+10.3	4	267.60	+4.30	+1.3	1
254.50	−9.60	−1.7	1,2	262.20	−12.35	+5.2	1,2,3,6	267.70	−7.35	+1.5	4
255.30	−4.90	+9.8	1	263.00	−12.00	+3.8	1	267.70	−7.35	+5.3	1,3,4,5
255.50	−4.80	+10.5	1	263.95	−11.70	+4.0	1,2	267.90	−7.80	+6.5	1,5
255.79	−9.18	−4.5	2	264.40	−6.30	+6.3	4	268.10	−9.50	+6.1	1
255.83	−6.59	+10.9	4	264.42	+5.71	+10.1	1,4	268.10	−7.50	+3.9	2
256.10	−10.50	−2.2	2	264.42	+5.71	+5.4	4	268.20	−9.70	+5.9	1
256.10	−9.30	−4.3	1	264.50	−11.30*	+12.0	1	268.20	−9.50	+5.5	1
256.10	−9.10	−5.2	1	264.50	+5.00	+2.5	1	268.20	−8.90	+4.8	1
256.20	−12.38	−1.7	2	264.50	+5.60	+10.0	1	269.50	−7.60	+4.8	1
256.26	−5.60	+9.6	4	265.35	+5.35	+3.3	1	269.50	+4.00	−3.8	1
256.40	−10.00	−3.6	1	265.38	−9.75	−6.7	4	269.90	−11.10	+0.8	1
256.90	−10.40	−4.5	1	265.60	−6.50	+5.6	4	269.90	−11.10	−0.5	1
256.90	−5.40	+11.3	1	265.60	−6.00	+5.0	2	270.10	+4.20	−3.8	1
257.20	−10.30	−3.6	1,5	265.70	−7.70	+2.9	1,5	270.75	−4.45	+2.2	2
258.08	−4.00	+10.2	4	265.70	−5.00*	+1.3	4	270.80	−8.50	+0.8	1,2
258.08	−4.00	+11.5	4	265.80	−7.40	+3.4	1,4,6	270.80	−8.50	−0.6	1,2
258.20	−4.50	+13.0	4	266.00	−8.50	+3.7	4	271.40	+4.80	−3.2	1,3
258.20	−4.50	+8.1	4	266.00	−7.50	+3.5	1	271.78	+4.88	−3.0	3
258.54	+8.13	+2.1	4								

[a] 1: Otrupcek et al. 2000 2: this work, HartRAO 3: Goss et al. 1980 4: this work, Mopra 5: Bourke et al. 1995 6: de Vries et al. 1984 7: Sridharan 1992

Table 4. Cometary globule positions and velocities, from the literature.

identity	l [°]	b [°]	v_{lsr} [km s^{-1}]	references[a]	identity	l [°]	b [°]	v_{lsr} [km s^{-1}]	references
CG37	251.11	+0.52	+6.2	1	CG8	255.06	−8.76	−5.8	1,5
CG27	251.67	+0.15	+5.0	1,2	CG2	255.32	−14.35	+4.1	1,2,3,4,5
CG28	251.80	+0.05	+5.2	1	CG10	255.79	−9.18	−5.5	1,5
CG29	251.88	+0.01	+5.2	1	CG1	256.14	−14.07	+3.3	1,2,3,5
CG26	252.15	+0.73	+2.0	1,2	CG36	256.95	+2.65	−8.5	1
CG33	252.29	+0.51	+1.6	1	CG5	257.18	−10.27	−3.4	2
CG32 B	252.48	+0.08	+4.8	1	CG6	258.99	−13.21	+0.9	1,2
CG32	252.51	+0.07	+4.85	2	CG4	259.48	−12.73	+1.7	1,2,4,5,6
CG32 A	252.52	+0.08	+4.9	1	CG13	259.48	−16.43	+3.7	1,2,3,4,5
CG31 C	253.11	−1.73	+6.3	1,2	CG24	260.02	−3.83	−12.5	1,2
CG31 D	253.11	−1.80	+6.9	1	CG25	260.65	−12.71	−1.8	1
CG31 B	253.18	−1.72	+6.0	1,2	CG3	260.72	−12.40	+0.1	1,2,5
CG31 A	253.19	−1.66	+6.0	1,2,3,4	CG14	262.49	−13.37	−0.9	1,2,3,5
CG30	253.29	−1.61	+5.8	1,2,3,4	CG16	262.86	−15.48	−0.7	1,2,5
CG22 B2	253.37	+3.24	+6.8	1	CG15	262.88	−14.67	−0.8	1,2,5
CG38	253.38	−1.64	+7.0	1	CG7	266.04	+4.31	−1.1	1,4
CG22 B1	253.58	+2.96	+6.5	1,2,3	CG18	269.67	−3.92	+2.0	1
CG34	253.82	−10.91	−1.0	2	CG17	270.59	−4.69	+3.7	1,5
CG9	255.06	−9.17	−4.2	1,5					

[a] 1: Sridharan 1992, 2: Bourke et al. 1995, 3: Zealey et al. 1983, 4: Goss et al. 1980, 5: Otrupcek et al. 2000, 6: de Vries et al. 1984

Table 5. The ranges and intervals of the parameters tested with the uniformly expanding shell model.

parameter	minimum	maximum	interval
$l/[°]$	250.0	270.0	0.5
$b/[°]$	−15.0	+10.0	0.5
$D/[\mathrm{pc}]$	0	1000	50
$\theta/[°]$	5.0	20.0	0.5
$v_{exp}/[\mathrm{km\ s^{-1}}]$	4	22	0.5

Table 6. The parameter values giving the minimum reduced χ^2 when fitting a uniformly expanding shell to the three data sets.

data	l [°]	b [°]	D [pc]	θ [°]	v_{exp} [km s^{-1}]	χ^2
DMC	260.0	−2.0	200	11.0	10.0	1.886
CG	261.5	−4.0	400	10.0	14.0	1.077
DMC+CG	260.5	−2.5	100	10.5	10.5	1.883

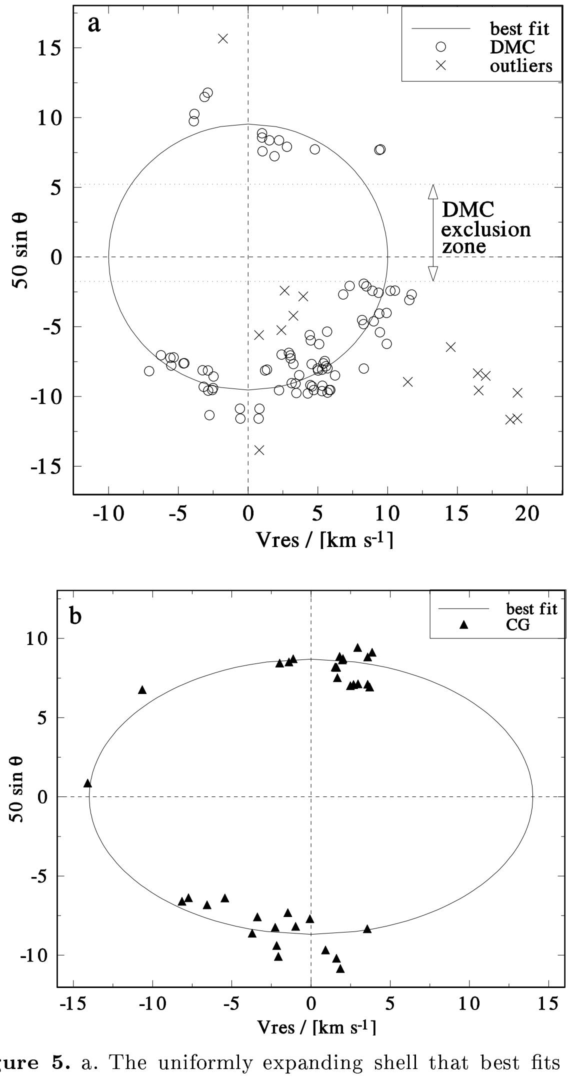

Figure 5. a. The uniformly expanding shell that best fits the DMC data set, excluding outliers, is shown as a function of sinθ (scaled by fifty) and v_{res}. b. The uniformly expanding shell that best fits the CG data set. These may be compared with Fig. 4a.

separate objects along the line of sight. However the distance to the centre is only a weak function of the model parameters, and the plot of χ^2 versus distance (Fig. 6a) shows that a large distance range is possible for both data sets. For the DMCs distances up to ∼600 pc are within 1 σ of the minimum. The 1-σ confidence level for the CGs lies beyond 1 kpc indicating that the distance constraint on the CGs is very poor. This suggests that the two data sets sample parts of the same object. This is further supported by the best-fit angular radii of the two data sets, which are within a degree of each other (Table 6) as well as lying within each other's 1-σ boundaries (Fig. 6b).

It is the expansion velocities of the two data sets that is the most difficult to reconcile. Fig. 6c shows that although the best-fit expansion velocity for the DMCs occurs just within the 1-σ level of that for the CGs, the same is not true for the best-fit expansion velocity of the CGs relative to the DMCs. As the extreme front face is poorly sampled in both data sets, the difference may not be that significant.

The balance of the evidence indicates that the DMCs and CGs form part of the same expanding shell. That this is reasonable is supported by the best-fit expansion centre positions. For the DMCs and CGs independently these are 2.5° apart, but the significance of this difference is only 1 σ, as shown in Fig. 7. If the data sets are combined, the best-fit uniformly expanding shell appears as in Fig. 8, and shows the similarity of the two data sets. The parameters for this fit are listed in Table 6.

As the data points are scattered about the mean angular radius, an outer radius defining the outline of this neutral shell is given by the maximum absolute value of θ of the data points. This value is ∼14°. This outline is shown in Fig. 9 together with the positions of the DMC and the CG data. It is clear that the neutral shell is much larger than the IVS, but slightly smaller than the extent of the ionized gas in the Gum nebula. Even though poorly sampled by the line data at positive galactic latitudes, the neutral shell obviously extends into this region of sky. The data at positive galactic latitudes follows the expansion model well as shown by the points with positive sin θ in Fig. 8. The material at positive galactic latitudes evidently shares the overall motion of the material at negative galactic latitudes.

Fig. 10 shows the contour plot of χ^2 versus centre position for the combined DMC+CG data, for comparison with the DMCs and CGs separately, in Fig. 7. In all three cases, the centres of the best fit expanding shells are significantly closer to the geometric centre of the Gum nebula than to the centre of the IVS. However it is necessary to examine whether a separate expanding shell fits the subset of the data within the IVS.

5.4 Modelling the IRAS-Vela shell

A subset of the data, comprising those DMCs and CGs within 10° of the centre of the IVS at G263−7 (Sahu 1992) were tested for evidence of an expanding shell. These data cover a larger area than the 8° radius of the IVS, in order that the shell radius was less constrained while searching parameter space.

A search without constraints on the model parameters, other than that the centre position should lie within the proposed extent of the IVS, produced an expansion centre

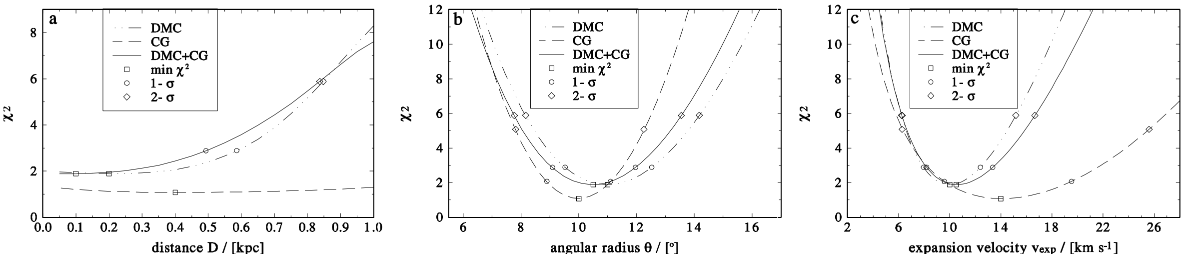

Figure 6. Variation in the χ^2 as a function of a. the distance to the expansion centre, b. the angular radius θ and c. the expansion velocity v_{exp} for the DMCs, the CGs, and the combined data. The expansion centre position was fixed at that obtained for the minimum χ^2. For a. the best fit for each distance was determined, while for b. and c. only one parameter, the angular radius and the expansion velocity respectively, was varied. The χ^2 minima, and the 1- and 2-σ confidence levels are shown.

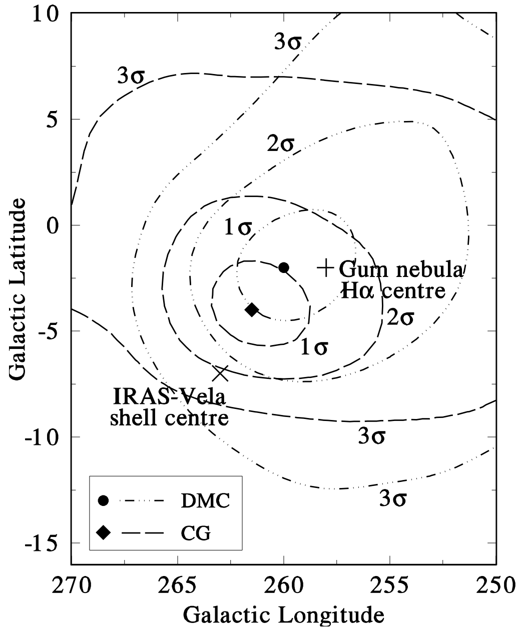

Figure 7. Contour plot of the reduced χ^2 as a function of the expansion centre position, obtained from fitting a uniformly expanding shell to the DMC data and to the CG data. The diamond and filled circle give the positions of the minimum χ^2 for each data set. The contours show the 1σ, 2σ and 3σ boundaries above the minimum χ^2 positions.

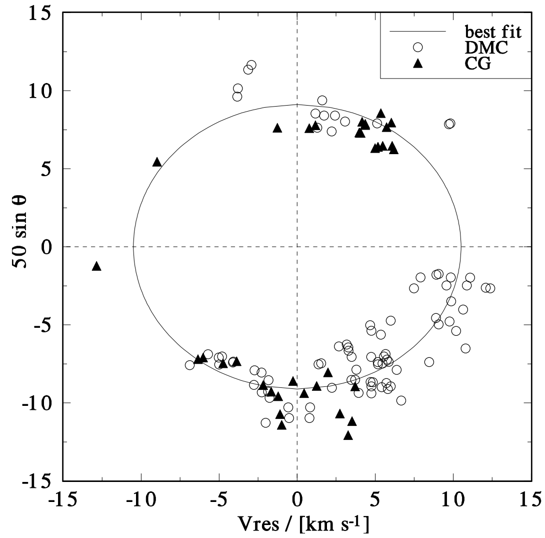

Figure 8. The uniformly expanding shell that best fits the combined data.

at G260.5−4.5 (Table 7 row 1). This is only 2° from the expansion centre obtained for the full DMC + CG data set as listed in Table 6, but 3.5° from the IVS centre.

Fixing the parameters to those derived for the neutral shell of the complete DMC+CG data given in Table 6, gives a fit that is only slightly worse (Table 7 row 2). This indicates that the IVS subset of the DMC+CG data within 10° of the IVS centre still fits a shell centred at G260.5−2.5 fairly well and better than it fits a shell with the IVS parameters, as shown below.

For comparison, the remaining rows of Table 7 gives the best-fit results for an IVS centre fixed at G263−7 with different combinations of constraints. Row 3 tests the fit if the IVS is placed at the distance of γ^2 Velorum determined by Hipparcos. With $\chi^2 > 4$ the fit is not convincing compared to the first two solutions. In row 4 the goodness of fit is tested for the IVS placed at the Vela OB2 association, and the fit is again poor. In row 5 only the shell centre is fixed,

Table 7. The parameter values giving the minimum reduced χ^2 when fitting a uniformly expanding shell to the IVS data subset, for a range of constraints on shell parameters.

	fixed parameters	Centre $[l, b]$	D [pc]	θ [°]	v_{exp} [km s^{-1}]	χ^2
1	none	260.5−4.5	150	9.0	10.0	1.60
2	l, b, D, θ, v_{exp}	260.5−2.5	100	10.5	10.5	1.64
3	l, b, D, θ, v_{exp}	263.0−7.0	260	8.0	10.0	4.24
4	l, b, D, θ, v_{exp}	263.0−7.0	410	8.0	10.0	4.56
5	l, b	263.0−7.0	200	7.0	10.5	3.95

to match the centre of the IVS. While the fit is a little better than for the previous two rows, it is still poor compared to that of rows 1 and 2.

Fig. 11a shows the unconstrained fit to the IVS data (Table 7 row 1), and for comparison Fig. 11b shows the best fit for a centre position at G263.0−7.0 (Table 7 row 5). The latter is clearly a poor solution compared to the former. While the unconstrained fit is acceptable, it is obtained with a subset of the DMC+CG data whose selection cannot be justified if it does not produce a good fit for the IVS centre, which it does not.

We conclude that the IVS is not distinguishable from the neutral shell shown in Fig. 8 and that the CGs are part

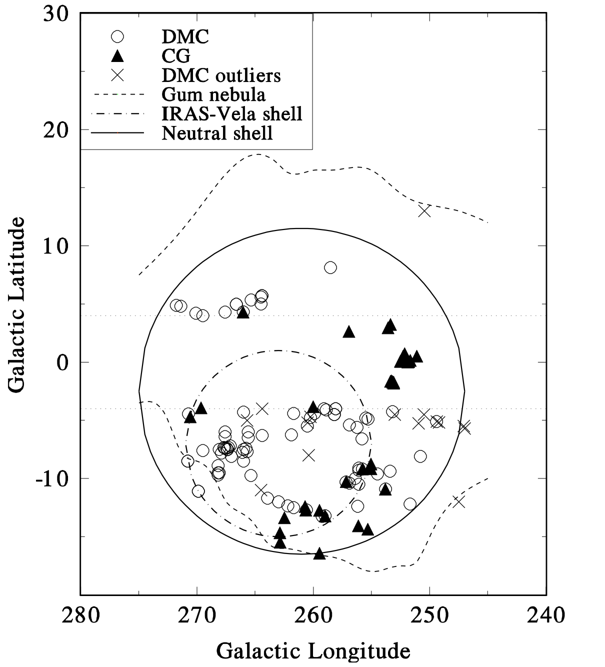

Figure 9. The positions of the DMCs, DMC outliers and CGs are shown together with the outlines of the Gum nebula at 2.3 GHz (Jonas et al. 1998), the IVS, and the maximum extent of best fit symmetric expanding shell fitted to the DMC+CG data.

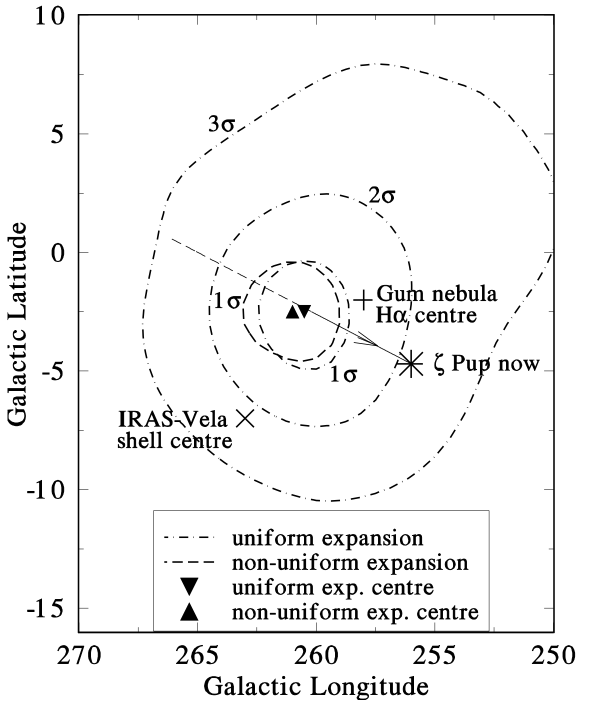

Figure 10. Contour plot of the reduced χ^2 versus centre position for uniformly and non-uniformly expanding shells fitted to the combined data. The solid symbols give the positions of the minimum χ^2 for the two models. The path of ζ Puppis across the sky over the last 4 Myr is shown as a dashed then solid line.

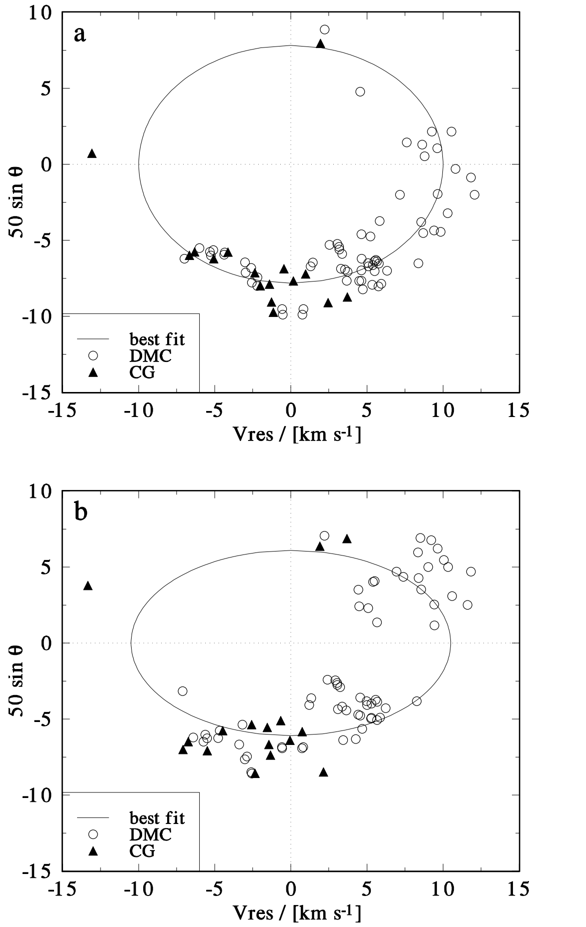

Figure 11. Fits of the uniformly expanding shell model to the IVS data subset. a. The best fit unconstrained uniformly expanding shell (Table 7 row 1). b. The best fit uniformly expanding shell constrained to have a centre at G263−7 (Table 7 row 5).

of the expanding neutral shell rather than the IVS. Thus the IVS does not manifest itself in these molecular line data as a separate expanding entity.

We return therefore to further treating the full data set as a single entity, and examine the uniformity of the expansion found in section 5.3.

6 UNIFORMITY OF THE NEUTRAL SHELL EXPANSION

The uniform expansion model was found to be relatively insensitive to the distance to the neutral shell centre. The significance of the best-fit centre of the combined data being found at only 100 pc (section 5.3) is therefore not high. However this low distance could be a symptom of unmodelled non-uniform expansion.

The possibility of this non-uniformity was hinted at by the best-fit velocities obtained for separate DMC and CG data sets. For the CGs, which dominate the front face of the shell, an expansion velocity of 14 km s^{-1} was obtained, whereas the DMC data, which dominates the back face, gave an expansion velocity of only 10 km s^{-1}. Although the front face expansion velocity is almost totally determined by two data points of the CG data (Fig. 5b), these nevertheless have

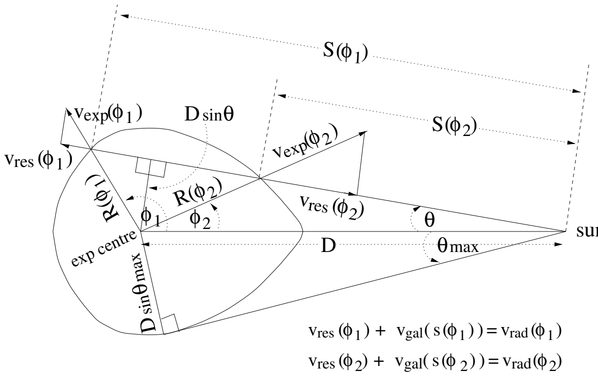

Figure 12. Schematic diagram of the viewing geometry of a spectral line observed at a position on the near or far face of a non-uniformly expanding shell.

to be regarded as representative of the front face motion, given the paucity of data on the front face.

The shell expansion model was therefore modified to permit different expansion rates for its front and back faces.

7 MODELS OF NON-UNIFORMLY EXPANDING SHELLS

7.1 Geometry of non-uniform expansion

The configuration of the non-uniform expansion is shown in Fig. 12. The expansion velocity, v_{exp}, is taken to be a simple function of ϕ, the angle measured at the shell centre between the line to the cloud and the line of sight to the observer. v_{exp} is directed radially outwards from the expansion centre. For consistency, the radius is also taken to be a function of ϕ. The form of the two functions is:

$$R(\phi) = R_b + (R_f - R_b)[(180.0 - \phi)/180.0]^2 \quad (7)$$

$$v_{exp}(\phi) = v_{exp,b} + (v_{exp,f} - v_{exp,b})[(180.0 - \phi)/180.0]^2 \quad (8)$$

where R_b and R_f are the minimum and maximum radii and $v_{exp,b}$ and $v_{exp,f}$ are the minimum and maximum expansion velocities. The minima occur at the back of the shell and the maxima at the front.

From the geometry shown in Fig. 12 in the non-uniform case Equation 1 for uniform expansion becomes:

$$v_{res}(\phi) = \pm v_{exp}(\phi)(1 - D^2 \sin^2\theta / R^2(\phi))^{\frac{1}{2}} \quad (9)$$

Solving for $\sin\theta$ in Equation 9 we obtain:

$$\sin\theta = \pm(R(\phi)/D)(1 - v_{res}^2(\phi)/v_{exp}^2(\phi))^{\frac{1}{2}}. \quad (10)$$

Fitting this model to the data had to be done numerically. Nevertheless the steps of the numerical process were similar to the analytical steps used for the uniformly expanding shell model.

If the expansion centre lies at a distance D, then $S(\phi)$, the distance to the position on the shell, is derived from simple geometric arguments, illustrated in Fig. 12, as

$$S(\phi) = (D^2 + R^2(\phi) - 2DR(\phi)\cos\phi)^{\frac{1}{2}}. \quad (11)$$

The contribution of the radial component of the galactic rotation to the observed radial velocity is then determined

Table 8. The ranges and intervals of model parameters for the non-uniformly expanding shell model. The parameters are the centre position, l, b, the distance to the centre, D, the expansion velocities of the front face, $v_{exp,f}$, and back face, $v_{exp,b}$ of the shell and the radii of the front face, R_f, and back face, R_b, along the centreline of the shell.

parameter	minimum	maximum	interval
l/[°]	257.0	264.0	0.5
b/[°]	−5.0	0.0	0.5
D/[pc]	0	700	100
$v_{exp,b}$/[km s^{-1}]	4.0	14.0	0.5
$v_{exp,f}$/[km s^{-1}]	8.0	21.0	0.5
R_b[a]/[pc]	5, 10, 15	20 to 225	5, 10, 15
R_f[a]/[pc]	10 to 90	45 to 450	5, 10, 15

[a] Values used depend on the distance to the expansion centre and were chosen to give intervals in the angular radius of the shell of 0.6° to 1.1°.

using the appropriate distance S given by Equation 11. Positions lying outside the shell boundary have $\theta > \theta_{max}$, and a distance of $D\cos\theta$ was then used, as in the case of uniform expansion.

7.2 Fitting a non-uniformly expanding shell

Guided by the results of the fit of the uniform expansion model, the best fit of the non-uniformly expanding shell to the combined DMC + GMC data set was determined for the reduced ranges of parameters listed in Table 8. The outlier rejection of the uniform shell was retained. The parameters giving the best fit are shown in the first row of Table 9 and may be compared with the uniform expansion fit results in Table 6. The fit is depicted in Fig. 13, for comparison with the uniform expansion fit shown in Fig. 8.

Both the uniform and non-uniform best fits give very similar angular radii for the shell, of 10.5° and 10.7° respectively. Both fits give outer radii of ~14°. Fig. 10 shows that the expansion centre positions and 1-σ uncertainty boundaries are very similar.

As expected, the non-uniform model gives different expansion velocities for the front and back faces (Table 9), which are consistent with the expansion velocities obtained from the CG and DMC data taken separately (Table 6), as the CGs dominate the front and the DMCs the back face. The radius of the non-uniform shell varies between 60 pc on the near side to 100 pc on the far side at the best-fit distance.

The variation in χ^2 with distance to the expansion centre in the two models is compared in Fig. 14. The additional free parameters in the non-uniform model produces a less constrained, but more plausible result, the best fit distance being 400 pc with plausible limits of 200 to 500 pc. Next we examine arguments that may help to refine this distance.

7.3 The distance to the expansion centre

The kinematic distance range found from the non-uniform expansion model encompases the distances to the Vela OB2 association (410 pc - De Zeeuw et al. 1999), γ^2 Velorum (258 pc - van der Hucht et al. 1997, or 410 pc - Pozzo et al.

Table 9. The parameters obtained from best fit of the non-uniformly expanding shell model to the combined data set. The best fit is given in the first row. The best fit for the same centre position as in the first row but at a distance of 500 pc is given in the second row.

l [°]	b [°]	D [pc]	R_{min} [pc]	R_{max} [pc]	θ [°]	$v_{exp,min}$ [km s^{-1}]	$v_{exp,max}$ [km s^{-1}]	χ^2
261.0	-2.5	400	60	100	10.7	9.0	13.0	1.837
261.0	-2.5	500	70	130	10.5	8.5	14.0	1.881

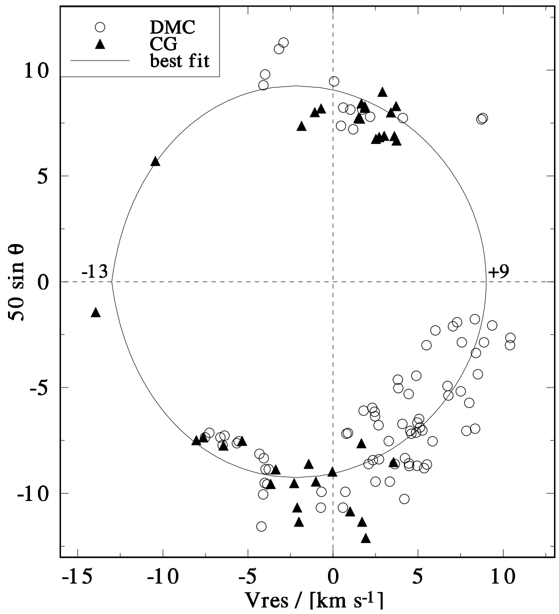

Figure 13. The best fit of a non-uniformly expanding shell model to the combined data set.

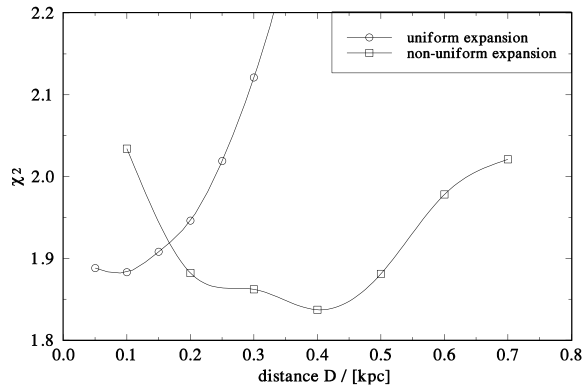

Figure 14. χ^2 as a function of distance for both the uniform and non-uniform models with the centre positions fixed at those given by the minimum χ^2 for each model.

2000) and the runaway O star ζ Puppis - (429^{+120}_{-77} pc - van der Hucht et al. 1997).

None of these have current positions that match the shell expansion centre found from the modelling. However, the Hipparcos values for the peculiar motion of ζ Puppis given in table 1 of Moffat et al. (1998) can be used to project its motion backwards in time. This path is shown in Fig. 10. It passed within the 1-σ boundary of the shell centre 2.5 Myr ago and left it 0.9 Myr ago. It passed within $< 0.5°$ of the expansion centre 1.5±0.4 Myr ago. At this time ζ Puppis was about 500^{+140}_{-95} pc distant, matching the largest estimate of the distance for the expansion centre.

van Rensbergen, Vanbeveren & de Loore (1996) have investigated several scenarios for the origin of the runaway O-star ζ Puppis. Most likely is that ζ Puppis was in a binary system of (40+36)$M_\odot$, in which the more massive component underwent a supernova (SN) explosion [0.9 - 2.0] Myr ago, leading to the runaway of ζ Pup. This agrees with the timespan during which its path was closest to the centre of the neutral shell. Adopting the hypothesis that the SN and the expanding shell are indeed causally related, we set a distance of 500 pc to the expansion centre and a time of 1.5 Myr since the SN. The best-fit parameters given for this distance by the non-uniform model are listed in row two of Table 9.

Next we investigate the connection between the neutral shell studied above and the Hα and radio emission that has historically been identified as the Gum nebula.

8 DISCUSSION

Hydrogen recombination lines have been detected at radio wavelengths from the Gum nebula (Woermann, Gaylard & Otrupcek 2000), which is therefore at least partly photo-ionized. However, Woermann et al. (2000) also showed that their data are consistent with the presence of a mixture of thermal and synchrotron radio emission. Such a mixture was also reported by Duncan et al. (1996) from radio polarization and total power maps of the Gum nebula region in the area close to the Galactic plane.

The presence of synchrotron radio emission over the full extent of the neutral shell helps to confirm the origin of the expansion of the neutral shell as due to interaction with an expanding supernova remnant. Synchrotron radio emission predominates over thermal emission at low radio frequencies. The 408 MHz radio emission (Haslam et al. 1982), depicted in greyscale form in Fig. 15a for this region, has the expansion centre and the mean and outer angular extent of the neutral shell superimposed. It is clear that the outer shell boundary is similar to the radio continuum boundary.

By contrast, the Hα emission from the Gum nebula (Chanot & Sivan 1983) comes primarily from photo-ionized gas. The extent of this emission is compared to the best fit neutral shell in Fig. 15b. Again the outer boundary of the neutral shell is well matched except at high positive galactic latitudes. Chanot & Sivan (1983) have shown that ζ Puppis on its own is capable of ionizing the Hα region known as the Gum nebula. Accepting a distance of 500 pc to the shell centre, the current position of ζ Pup is 70 pc in front of the expansion centre, which is within the 130pc front radius of the neutral shell. This is consistent with ζ Puppis being

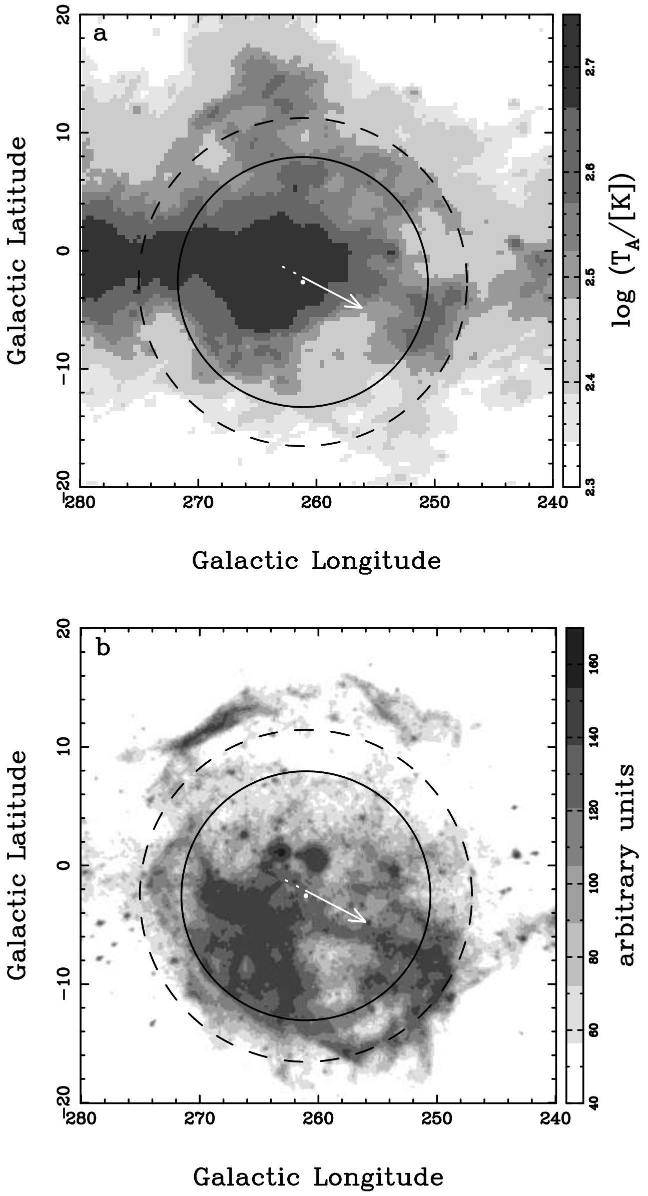

Figure 15. The mean and outer angular radius of the neutral shell superimposed on a. the 408 MHz radio continuum map (Haslam et al 1982). covering the Gum nebula region and b. the Hα emission from the Gum nebula (Chanot & Sivan 1982). The path of ζ Pup over the past 2.5 Myr is marked by the white arrow. The current position of ζ Puppis is at the arrowhead. The white dot is the centre of the neutral shell given by the non-uniformly expanding shell model.

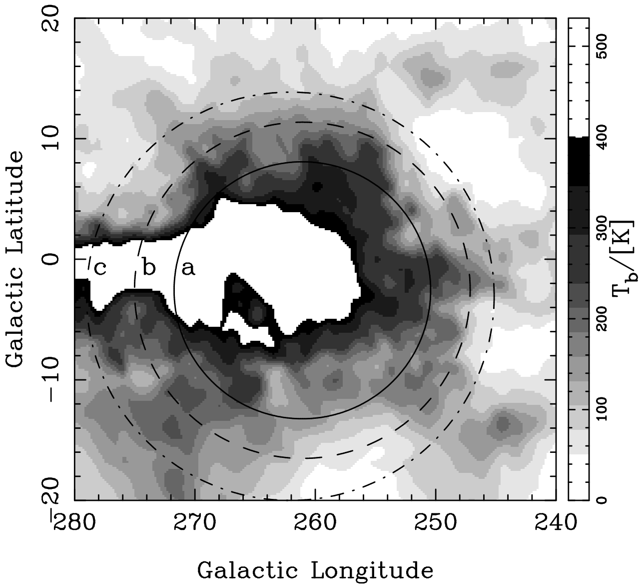

Figure 16. The mean (a) and outer (b) angular radii of the neutral shell superimposed on the HI emission from the Gum nebula region integrated between 0 and 10 km s^{-1} (Reynoso & Dubner 1997). The giant HI disk dimensions (c) are also shown.

the primary source of the UV photons that maintain the photo-ionization.

Fig. 15b shows that the two Hα emission features above $b > 10°$ lie well above the neutral shell and puts their relationship to the Gum nebula into question. The OH 1667 MHz line detected at G250.45+13.6, which is in the direction of the upper right Hα feature, was found to be an outlier with a velocity of -0.3 km s^{-1}, indicating that this is probably a nearby cloud with some peculiar motion towards us, that is ionized by the UV flux of ζ Pup or γ^2 Vel. This scenario is supported by the detection an Hα line at -1.6 km s^{-1} and a [NII] line at -0.8 km s^{-1} towards G249.2+12.2, in the same feature, by Reynolds (1976a). At this position differential galactic rotation for material at 500 pc would produce a radial velocity of $+4.3$ km s^{-1}. The feature at G269+11 may be the brightest portion of a large, faint shell centred at G275+20 with angular radius of 11° (McCullough et al. 2000). A portion of this shell can be seen in the 2.3 GHz survey (Jonas et al. 1998, shown in fig. 1 of Woermann et al. 2000). The scenario outlined here for these two regions may well be more complex but they are difficult to interpret as their emission at all wavelengths is very faint. We conclude that the outer boundary of the neutral shell may represent the real perimeter of the Gum nebula, giving it a significantly smaller size than that suggested by Chanot & Sivan (1983).

Reynoso & Dubner (1997) showed that there is an HI hemisphere in this region of sky, which they called the 'giant HI disk'. It is centred at G262$-$3 and has a diameter of $\sim$34°. In Fig. 16 the best fit and outer edge of the neutral shell are shown superimposed on the HI integrated between 0 and +10 km s^{-1} (fig. 3 of Reynoso & Dubner 1997), with the 'giant HI disk' outlined. Most of the confusing parts along the plane as well as another feature, the 'thick HI shell', have been excluded by setting their display values to white. The neutral shell is smaller than the giant HI disk. The highest positive velocities found in the DMCs (Table 3) are in the range +10 to +13 km s^{-1}, which occur close to the centre of the neutral shell near the galactic plane and are obscured by the velocity components of the 'thick HI shell'. While there is too much confusion to determine the positive velocity limit of the giant HI disk, its concentricity and overlap in velocity with the DMCs and CGs suggests that it forms an outer shell to the back face of the DMC+CG shell.

The balance of the evidence indicates that the neutral shell, the radio synchrotron emission, the Hα emission from thermal ionized gas and the giant HI disk are all connected.

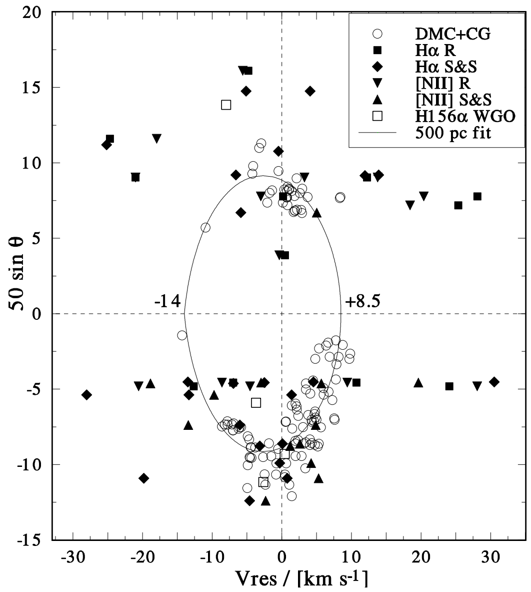

Figure 17. The best fit non-uniform shell at 500 pc with the molecular line, optical (R: Reynolds 1976a; S&S: Sahu & Sahu 1993) and the H156α recombination lines of Woermann et al. (2000) superimposed.

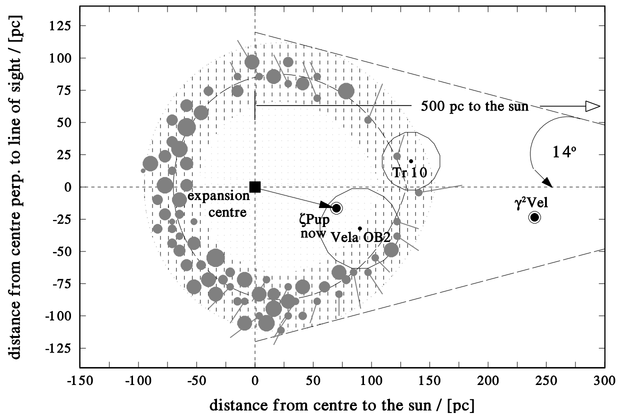

Figure 18. Cartoon of the clumpy neutral shell around the Gum nebula, the Vela OB2 and Trumpler 10 star associations, γ^2Velorum, and the path of the runaway star ζ Puppis. The lengths of the CG tails are exaggerated for clarity.

Their origin is best explained by the model first proposed by Reynolds (1976b), i.e. a 1 Myr old supernova remnant with an expanding photo-ionized shell.

Optical line emission from the Gum nebula should then follow the same expansion model as the DMC+CGs, as the UV photon flux would partly ionize the neutral material. (Fig. 17) shows the [NII] and Hα line data of Sahu & Sahu (1993) and Reynolds (1976a, fig. 3) compared to the non-uniform expanding shell at 500 pc. Approximately half the optical data fall within the bounds of the neutral shell, the remainder showing more extreme velocities. The latter are likely to be from high velocity filaments in the nebula. The neutral material shows a much more convincing expansion pattern.

The H156α lines (Woermann et al. 2000) shown in Fig. 17 do not exhibit the extreme velocities of the optical data, probably owing to the averaging effect of the relatively large telescope beam, 30′ field of view versus 1′ (Sahu & Sahu 1993) and 6′ (Reynolds 1976a), the sensitivity of the radio recombination line data to cooler rather than hotter gas and the high accuracy of radio doppler velocity measurements, which have a resolution typically of 1 km s^{-1} compared to 7.5 km s^{-1} (Sahu & Sahu 1993) and 12 km s^{-1} (Reynolds 1976a). The recombination line detected at G270.65+10.4 gives further weight to the possibility that the Hα feature around G269+11 may not be part of the Gum nebula as it lies far above the best fit neutral shell in Fig. 17.

The likely configuration of the main objects in the region is illustrated in Fig. 18. ζ Puppis is located inside the Gum nebula, near its front face, and provides most of the photo-ionizing flux. The Vela OB2 association is situated within the front face and also contributes to the photo-ionization. If the Hipparcos distance to γ^2Velorum is adopted (as shown), it lies well in front of the nebula and neutral shell, but if Pozzo et al. (2000) are correct in revising this distance, then it is also situated within the front face of the nebula and neutral shell. The distribution of neutral material over the front face of the neutral shell is very patchy. This may reflect its initial distribution, or it may be a product of the photo-ionization.

The size of the nebula and shell if 500 pc distant raises the question as to whether a single SN has the energy to produce it, or whether a supershell resulting from multiple SNe must be invoked. The latter was proposed McCray (1988) and Reynoso & Dubner (1997), based on the equations of Shull (1987). These were derived assuming that the SNR merges with the surroundings when it reaches an expansion velocity of 20 km s^{-1}. However, the neutral shell and Gum nebula are still distinct from their surroundings, although expanding at only half this velocity. Thus we rather use equation 12 of McKee & Ostriker (1977) with R_c given by their equation 9, resulting in

$$R = 2.117 E_{51}^{\frac{1}{7}} n_o^{-\frac{1}{7}} t^{\frac{2}{7}} \qquad (12)$$

for the radius R of a supernova remnant at time t yr after the SN explosion in a medium of density n_o (cm^{-3}). E_{51} (10^{51} ergs) is the kinetic energy released in the SN explosion and is canonically taken to be 1 but may be as large as 3.

Estimates of the ambient density of the ISM in the Gum nebula region range from $\sim$0.1 cm^{-3} to $\sim$1 cm^{-3} (Brandt et al. 1971; Wallerstein & Silk 1971; Bohlin, Savage & Drake 1978; Vidal 1979; Manchester & Taylor 1981; Lyne, Manchester & Taylor 1985; Taylor & Cordes 1993; Oberlack et al. 1994; Reynoso & Dubner 1997) This gives a range of 1.0 to 1.4 to $n_o^{-\frac{1}{7}}$. Using a radius of 120 pc and E_{51} of 1, equation 12 then gives a time of 0.42 to 1.4 Myr since the SN, for the ambient density range of the ISM in the region. This is consistent with the time derived from the backward projected path of ζ Puppis. Hence there is no compelling reason to postulate a supershell origin for the Gum nebula.

9 CONCLUSIONS

We have shown that the diffuse molecular clouds in the Gum nebula region and the cometary globules are part of the same expanding shell. Although these data are fitted well by a uniform expansion model, a more plausible distance to the expansion centre is obtained when a non-uniformly expanding shell model is used, in which the front face expands faster than the back face. Both versions give similar positions for the expansion centre and angular radius of the neutral shell.

We show that the runaway O-star ζ Puppis was within $< 0.5^\circ$ of the expansion centre of the neutral shell $\sim$1.5 Myr ago. The evidence suggests that the SN explosion of the erstwhile binary companion of ζ Puppis and the expansion of the neutral shell are causally related. Thus we adopt a distance of 500 pc to the expansion centre of the shell. The centre of the shell is at G261$-$2.5, the mean angular radius is 10.5°, the front face radius and expansion velocity are 130 pc and 14 km s^{-1} respectively and the back face radius and expansion velocity are 70 pc and 8.5 km s^{-1} respectively.

The outer dimension of the neutral shell is 14°. It covers all the Hα emission of the Gum nebula, excepting those at galactic latitudes $> +10^\circ$, which may be unrelated to the Gum nebula. The SN origin of the Gum nebula is confirmed by its radio emission. The Hα emission evidently comes from swept up material ionized by ζ Puppis, which is inside the shell. A single SN is capable of having formed this shell and thus the model of Reynolds (1976b) is appropriate for the Gum nebula, but with a somewhat slower expansion velocity and with γ^2 Velorum lying outside the shell. We found no evidence in these data for the IRAS-Vela shell as a separate expanding shell, and we suggest that it is a density enhancement in the neutral shell.

REFERENCES

Bohlin R.C., Savage B.D., Drake J.F., 1978, ApJ, 224, 132
Brandt J.C., Stecher T.P., Crawford D.L., Maran S.P., 1971, ApJ, 163, L99
Bourke T.L., Hyland A.R., Robinson G., James S.D., Wright C.M., 1995, MNRAS, 276, 1067
Chanot A., Sivan J.P., 1983, A&A, 121, 19
de Vries C.P., Brand J., Habing H.J., Israel F.P., de Graauw Th., Wouterloot J.G.A., van de Stadt H., 1984, A&AS, 56, 333
de Zeeuw P.T., Hoogerwerf R., de Bruijne J.H.J., Brown A.G.A., Blaauw A., 1999 AJ, 117, 354
Duncan A.R., Stewart R.T., Haynes R.F., Jones K.L., 1996, MNRAS, 280, 252
Feitzinger J.V., Stüwe J.A., 1984, A&AS, 58, 365
Fich M., Blitz L., Stark A.A., 1989, ApJ, 342, 272
Gum C.S., 1952, Observatory, 72, 151
Goss W.M., Manchester R.N., Brooks J.W., Sinclair M.W., Manefield G.A., Danziger I.J., 1980, MNRAS, 191, 533
Hartley M., Tritton S.B., Manchester R.N., Smith R.M., Goss W.M., 1986, A&AS, 63, 27
Haslam C.G.T., Stoffel H., Salter C.J., Wilson W.E., 1982, A&AS, 47,1
Hippelein H.H., Weinberger R., 1975, A&A, 43, 405
Jonas J.L., Baart E.E., Nicolson G.D., 1998, MNRAS, 297, 977
Lyne A.G., Manchester R.N., Taylor J.H., 1985, MNRAS, 213, 613
Manchester R.N. Taylor J.H., 1981, AJ, 86, 1953
Murphy D.C., May J., 1991, A&A, 247, 202
McCray R., 1988, in Roger R.S., Landecker T.L., eds, Supernova Remnants and the Interstellar Medium (IAU Coll. 101). Cambridge University Press, Cambridge, 447
McCullough P.R., Gaustad J., Rosing W., Van Buren D., 2000, Poster at "The Fourth Tetons Summer Conference: Galactic Structure, Stars and the Interstellar Medium." Grand Teton National Park, Jackson Hole, Wyoming USA
McKee C.F., Ostriker J.P., 1977, ApJ, 218, 148
Moffat A.F.J. et al., 1998, A&A, 331, 949
Oberlack U., Diehl R., Montmerle T., Prantzos N., von Ballmoos P., 1994, ApJS, 92, 433
Otrupcek R.E., Hartley M., Jung-Sheng W., 2000, PASA, 17, 92
Pozzo M., Jeffries R.D., Naylor T., Totten E.J., Harmer S., Kenyon M., 2000, MNRAS, 313, L23
Press W.H., Teukolsky S.A., Vetterling W.T., Flannery B.P., 1992, Numerical Recipes in Fortran The Art of Scientific Computing, Second Edition, Cambridge University Press
Reipurth B., 1983, A&A, 117, 183
Rajagopal J., Srinivasan G., 1998, JApA, 19, 79
Reynolds R.J., 1976a, ApJ, 203, 151
Reynolds R.J., 1976b, ApJ, 206, 679
Reynoso E.M., Dubner,G.M., 1997, A&AS, 123, 31
Shull J.M., 1987, in "Interstellar Processes", eds. D.A. Hollenbach and H.A.Thronson, Astrophysics and Space Science Library, D.Reidel Publ. Co., Dordrecht, Holland, 225
Sahu M.S., 1992, Doctoral Thesis, 'A study of the ISM in Puppis-Vela including the Gum nebula', Rijksuniversiteit Groningen, Netherlands
Sahu M.S., Sahu K.C., 1993, A&A, 280, 231
Sridharan T.K., 1992, JApA, 13, 217
Taylor J.H., Cordes J.M., 1993, ApJ, 411, 674
van der Hucht et al., 1997, NewA, 2, 245
van Rensbergen W., Vanbeveren D., de Loore C., 1996, A&A, 305, 825
Vidal J.-L., 1979, A&A, 79, 93
Wallerstein G., Silk J., 1971, ApJ, 170, 289
Wallerstein G., Jenkins E.B., Silk J., 1980, ApJ, 240, 834
Wheelock S.L. et al., 1994, IRAS Sky Survey Altas: Explanatory Supplement, JPL Publication 94-11, Jet Propulsion Lab., California Inst. of Tech., Pasadena, CA.
Woermann B., 1998, Ph.D. thesis, 'Radio Observations of the Gum Nebula Region', Rhodes University, Grahamstown, South Africa
Woermann B., Gaylard M.J., Otrupcek R., 2000, MNRAS, 315, 241
Yamaguchi N., Mizuno N., Moriguchi Y., Yonekura Y., Mizuno A., Fukui Y., 1999, PASJ, 51, 765
Zealey W.J., Ninkov Z., Rice E., Hartley M., Tritton S.B., 1983, ApL, 23, 119